




# Impact Experiment on Asteroid (162173) Ryugu: Structure beneath the Impact Point Revealed by In Situ Observations of the Ejecta Curtain

Toshihiko Kadono<sup>1</sup> , Masahiko Arakawa<sup>2</sup>, Rie Honda<sup>3</sup>, Ko Ishibashi<sup>4</sup>, Kazunori Ogawa<sup>2,5</sup>, Naoya Sakatani<sup>6</sup>, Hirotaka Sawada<sup>7</sup>, Yuri Shimaki<sup>7</sup>, Kei Shirai<sup>2</sup>, Seiji Sugita<sup>4,8</sup>, and Koji Wada<sup>4</sup>

<sup>1</sup> Department of Basic Sciences, University of Occupational and Environmental Health, Kitakyusyu, Japan; [kadono@med.uoeh-u.ac.jp](mailto:kadono@med.uoeh-u.ac.jp)

<sup>2</sup> Department of Planetology, Kobe University, Kobe, Japan

<sup>3</sup> Department of Science and Technology, Kochi University, Kochi, Japan

<sup>4</sup> Planetary Explosion Research Center, Chiba Institute of Technology, Narashino, Japan

<sup>5</sup> JAXA Space Exploration Center, Japan Aerospace Exploration Agency, Sagamihara, Japan

<sup>6</sup> Department of Physics, Rikkyo University, Tokyo, Japan

<sup>7</sup> Institute of Space and Astronautical Science, Japan Aerospace Exploration Agency, Sagamihara, Japan

<sup>8</sup> Department of Earth and Planetary Science, University of Tokyo, Tokyo, Japan

Received 2020 May 13; revised 2020 July 19; accepted 2020 July 22; published 2020 August 13

## Abstract

An impact experiment was performed on the surface of the C-type asteroid (162173) Ryugu using an instrument called the Small Carry-on Impactor (SCI) carried by the Japan Aerospace Exploration Agency spacecraft Hayabusa2. Using a small camera separated from the spacecraft, we observed the development of the ejecta curtain formed by the SCI impact in situ. Based on the patterns appearing in the ejecta curtain, we evaluated the physical properties of large boulders and regolith grains on Ryugu. We found that the large boulders on the surface near the SCI impact point had a compressive strength consistent with the previous estimation of a tensile strength based on low thermal inertia observed for boulders on Ryugu. Furthermore, the ejecta curtain consisted of the boulders with a maximum size of several decimeters. Moreover, the filament structure was formed in the SCI ejecta curtain, strongly suggesting that the SCI impact ejecta curtain particles had a size range greater than one order of magnitude; a characteristic size of the regolith grains in the curtain was estimated to be several centimeters. These regolith grains primarily originated from the subsurface layer. We propose three different hypotheses for the geological process that formed the subsurface structure at the SCI impact point consistent with the above observations. Because these hypotheses have different predictions for materials in SCI ejecta, the samples obtained from the second touchdown will be able to constrain which hypothesis is the most likely.

*Unified Astronomy Thesaurus concepts:* [Asteroids \(72\)](#); [Impact phenomena \(779\)](#); [Planetary science \(1255\)](#)

## 1. Introduction

Impact experiments in space have been conducted on a comet (DEEP IMPACT; e.g., A’Hearn et al. 2005) and the Moon (LCROSS; e.g., Colaprete et al. 2010) to study the structure beneath the impact point. In the DEEP IMPACT mission, based on the spatial variation in the color at mid-infrared wavelengths on the ejecta curtain, the materials of the subsurface of the comet Tempel 1 were found to be different from those of the surface (Kadono et al. 2007). In the LCROSS mission, the faint impact flash in visible wavelengths and the thermal signatures in the mid-infrared indicated a low-density surface layer (Schultz et al. 2010).

Recently, the Japan Aerospace Exploration Agency (JAXA) spacecraft Hayabusa2 explored the C-type asteroid (162173) Ryugu using remote-sensing measurements following its rendezvous in 2018 June (e.g., Sugita et al. 2019; Watanabe et al. 2019). In addition, Hayabusa2 performed an impact experiment using an instrument called the Small Carry-on Impactor (SCI) to study an impact crater formation process on an asteroid with actual materials at actual asteroid scales under microgravity; the crater-size scaling laws established in laboratories have consequently been verified (Arakawa et al. 2020).

One advantage of Hayabusa2 in this SCI experiment was the use of a small satellite separated from the spacecraft, the Deployable CAMera-3 (DCAM3), which was developed to observe the cratering process occurring on Ryugu due to the

SCI impact (Ogawa et al. 2017). This allowed us to observe the formation and development of the ejecta curtain in situ.

In this Letter, based on the observed pattern that appeared in the ejecta curtain, we evaluate the physical properties of the large boulders in the surface layer and the regolith grains in the subsurface layers of Ryugu. First, we describe the SCI impact experiment on Ryugu (Section 2). Then, in Section 3, we describe the pattern that appeared in the ejecta curtain and evaluate the strength of the large boulders on the surface, the maximum size of boulders in the curtain, and the size difference between large boulders and small regolith grains in the curtain. In Section 4, we discuss the subsurface structure beneath the SCI impact point (Section 4.1) and the formation process of this structure (Section 4.2).

## 2. Impact Experiment on Ryugu

The SCI operation was performed on 2019 April 5. The SCI body separated from Hayabusa2, and a hollow spherical copper projectile with a diameter of 13 cm, a mass of  $\sim 2$  kg, and a bulk density of  $\sim 1.7$  g cm<sup>-3</sup> was accelerated toward the surface of the asteroid. The impact velocity of the projectile at the surface of Ryugu was set to 2 km s<sup>-1</sup> (Arakawa et al. 2017; Saiki et al. 2017). The impact point was located in the northern area of the equatorial bulge, and a crater was successfully formed on Ryugu (Arakawa et al. 2020). DCAM3 operated normally and recorded images of the ejecta curtain growth caused by the impact at a distance of 1 km from the impact

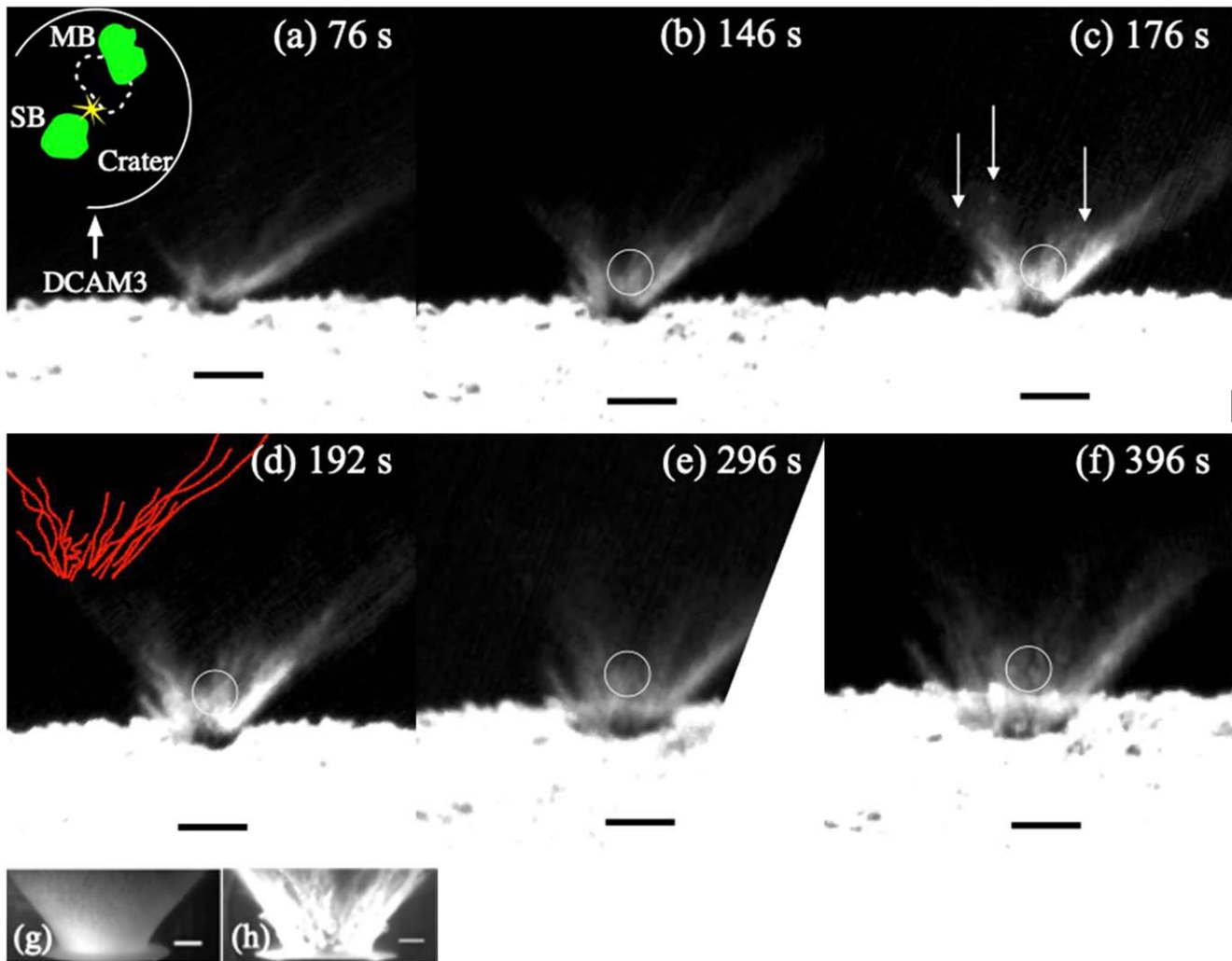


**Figure 1.** (a)–(f) Snapshots of the ejecta curtain observed by DCAM3. (a) 76 s after the impact (the configuration of the SCI crater and the line of sight of DCAM3 are schematically described in the inset; the scale is different from the ejecta curtain image), (b) 146 s, (c) 176 s (the arrows indicate the recognized boulders with several decimeters in size), (d) 192 s (filament structure can be recognized and is shown schematically in the inset), (e) 296 s (the right-hand side of the impact point was out of the field of view of the DCAM3 image), and (f) 396 s. The direction to the right-hand side in the images is north. The contrast in each image is changed to optimize the visibility of the ejecta curtain. The horizontal black scale bar in each panel indicates 20 m. The circle in the image in (b)–(f) indicates the area where we investigate the intensity to evaluate the spatial concentration of the regolith grains in the ejecta curtain. For comparison, we show the ejecta curtains obtained in the laboratory experiments for the targets consisting of (g) identical particles 0.1 mm in size (Kadono et al. 2020) and (h) mixed particles 0.1 mm and 4 mm in size (Kadono et al. 2019). The horizontal white scale bar in each panel indicates 5 cm.

point with a wide field of view of  $74^\circ \times 74^\circ$  and a high resolution of  $2000 \times 2000$  pixels, corresponding to a spatial resolution of less than  $1 \text{ m pixel}^{-1}$  (Ishibashi et al. 2017; Ogawa et al. 2017; Arakawa et al. 2020).

### 3. Results

Figures 1(a)–(f) show typical images taken by DCAM3 from 76 to 396 s after the impact. As described by Arakawa et al. (2020), from the beginning of the crater formation, the shape of the ejecta curtain was asymmetric (Figure 1(a)). Clear and extensive ejecta toward the right (north) were identified but such ejecta toward the left (south) were not observed. This is because the impact point was very close to a large boulder with sizes of several meters that was almost buried underground on the southeast side, denoted stable boulder (SB) in the inset of Figure 1(a). This inset schematically shows the top view of the SCI crater. The SCI crater was semicircular lacking the southeastern part, and its center was located very close to SB

(Figures 1, 2, and 4(b) in Arakawa et al. 2020). This suggests that the impact point was in the vicinity of SB. The boulder SB, which was not ejected by the SCI impact and might be deeply embedded, was an obstacle to the excavation flow and prevented the excavation flow from developing toward the southeast, permitting the materials to move only in a northward direction. As a result, the crater did not grow toward the southeast. On the other hand, another large boulder, mobile boulder (MB), near the impact point was moved by the SCI impact; MB could be transported by the excavation flow. Thus, the excavation flow might have extended beyond MB and come out on the far side of MB, resulting in an ejecta curtain. Consequently, the crater growth to the west side occurred.

Even though SB and MB were close to the impact point, there appeared to be no clear vestige of destruction due to the impact. This suggests that the SCI projectile collided not directly on these boulders but on the gap between them. Although the exact location of the SCI impact cannot be determined precisely, the fact that the distance between these

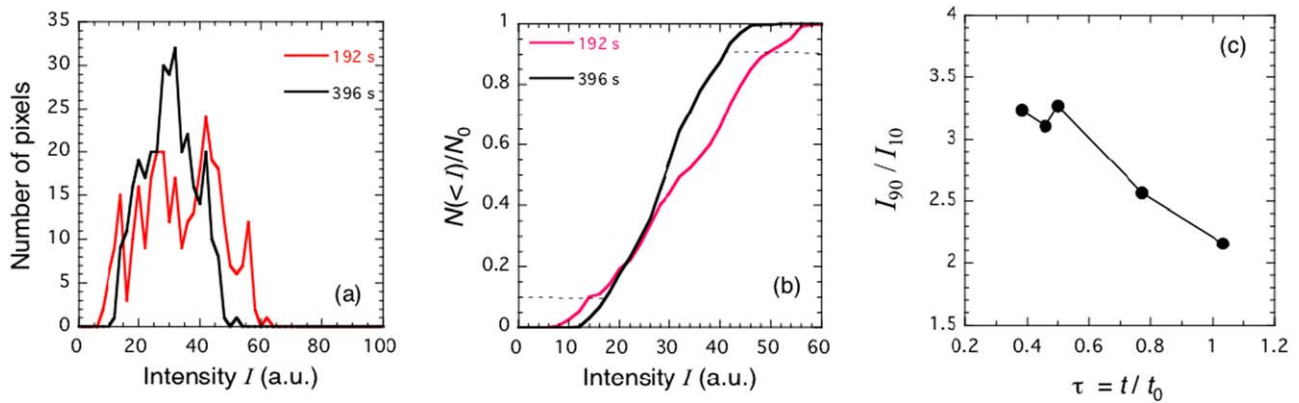


**Figure 2.** (a) Intensity distributions within an area with  $N_0 = 316$  pixels at 192 s (red curve) and 296 s (black curve) after the impact. (b) Cumulative number of pixels having an intensity lower than  $I$ ,  $N(<I)$ , normalized by  $N_0$  at 192 s (red curve) and 296 s (black curve). The horizontal broken lines indicate  $N(<I)/N_0$  values of 0.9 and 0.1. (c) The ratio of the intensities at  $N(<I)/N_0$  values of 0.9 and 0.1 as a function of the normalized time,  $\tau$ , defined by  $t/t_0$ , where  $t_0$  is set to  $3.8 \times 10^2$  s.

boulders prior to the SCI impact was  $\sim 1$  m means that either SB or MB is only  $\sim 0.5$  m away from the impact point. The dynamic pressure  $P$  caused by the SCI impact was estimated using Maxwell’s Z-model (Arakawa et al. 2020),  $\sim \rho(5.2/r^3)^2$ , where  $\rho$  and  $r$  are the density of the subsurface layer and the distance from the SCI impact point, respectively. When  $\rho = 10^3 \text{ kg m}^{-3}$ ,  $r = 0.5$  m results in pressures  $P$  of  $\sim 1.7$  MPa, and therefore the compressive strengths of SB and MB should be larger than this value. Because the compressive strength for ordinary rocks is generally larger about one order of magnitude than the tensile strength, this value is consistent with a tensile strength ( $\sim$ a few hundred kilopascals) estimated from the low thermal inertia observed by the Mobile Asteroid Surface Scout (MASCOT) for surface boulders (Grott et al. 2019).

Next, we consider a small structure of the ejecta curtain. At 146, 176, and 192 s (Figures 1(b)–(d)), the pattern of the ejecta curtain came to have a complex filament structure; the ejecta curtain was separated into two or more parts and was not straight but was undulating. The filament structure at 192 s is traced and shown in the inset in Figure 1(d). Laboratory experiments show that, when a target consists of particles that are identical in size, a small mesh pattern is observed in ejecta curtains (Kadono et al. 2015, 2020) as shown in Figure 1(g). Conversely, when the target consists of particles with a size range greater than one order of magnitude, various flow patterns in the ejecta are caused by the large-sized particles; as a result, the pattern of the ejecta curtain induced by an impact then exhibits high-contrast filament structures (Kadono et al. 2019) as shown in Figure 1(h). The complex filament pattern observed in the SCI ejecta curtain strongly suggests that the latter is the case. Note that some inhomogeneities originally existing in the ground of Ryugu may also cause such spatial variation in the ejecta curtain. However, because shock waves and subsequent excavation flows should smooth small inhomogeneities, the spatial variation due to small inhomogeneities would not appear in the curtain. Thus, the curtain was likely to consist of particles with a size range wider than an order of magnitude.

To evaluate the filament pattern quantitatively, we analyzed the pattern of the ejecta curtain in the images at 146, 176, and 192 s after the SCI impact using the same procedure as in Kadono et al. (2019). For comparison, the pattern of the ejecta curtain at the later stages at 296 and 396 s (Figures 1(e) and (f)) were also analyzed. We investigated the intensity within the

area of a circle with a diameter of 20 pixels (the total number of pixels within this circle was  $N_0 = 316$  pixels) and the circle was fixed at the same position of the ejecta curtain in each image, as shown in Figures 1(b)–(f). Figure 2(a) illustrates the intensity distributions at 192 s (red curve) and 396 s (black curve) after the impact. Figure 2(b) presents the cumulative number of pixels with intensities smaller than  $I$ ,  $N(<I)$ , which is normalized by  $N_0$  ( $=316$ ). To evaluate the intensity contrast, we considered the ratios of the intensities at  $N(<I)/N_0$  values of 0.9 and 0.1 (denoted  $I_{90}/I_{10}$ ). Figure 2(c) shows  $I_{90}/I_{10}$  for each shot as a function of the normalized time,  $\tau$ , which is time  $t$  after the impact divided by the characteristic timescale  $t_0$  defined as  $(D_c/g)^{1/2} = 3.8 \times 10^2$  s, where  $D_c$  is the rim-to-rim diameter of the SCI crater, 17.6 m (Arakawa et al. 2020), and  $g$  is the gravitational acceleration of Ryugu,  $1.20 \times 10^{-4} \text{ m s}^{-2}$  (Watanabe et al. 2019). Here, it is noted that Arakawa et al. (2020) defined a different crater formation timescale using the apparent crater radius 7.25 m and obtained  $2.5 \times 10^2$  s, whereas we used the rim-to-rim diameter according to the procedure developed in Kadono et al. (2019). For the ejecta curtain caused by the SCI impact,  $I_{90}/I_{10}$  is large ( $> \sim 3$ ) and then it rapidly decreases. Laboratory experiments by Kadono et al. (2019) show that, for targets containing both large inclusions and fine particles with the size ratio higher than at least one order of magnitude,  $I_{90}/I_{10}$  is large ( $> \sim 2.5$ ) and then it rapidly decreases. For the targets of identical particles,  $I_{90}/I_{10}$  is lower than  $\sim 2$  and then it gradually decreases. The result obtained from the SCI impact is consistent with the feature in the case of the targets consisting of large inclusions. Therefore, the ejecta curtain caused by the SCI impact likely included large boulders and small regolith grains with a size difference of at least one order of magnitude.

After 176 s, some individual boulders were recognized in the curtain (indicated by the three arrows in Figure 1(c)), whose sizes were  $\sim 2$ – $3$  pixels in the DCAM3 images. Because the point-spread function of DCAM3 was  $\sim 2$ – $3$  pixels (Ishibashi et al. 2017), the sizes of boulders were less than  $\sim 1$  pixel or  $\sim 1$  m. Their intensities were  $\sim 1/3$  of the SCI body prior to the impact (Figure S1 of Arakawa et al. 2020). Because the reflectance of the boulders should be lower ( $< \sim 1/10$ ) than that of the SCI body ( $\sim 0.8$ ), the sizes of the boulders would be larger than the SCI body (approximately 30 cm) and on the order of several decimeters, which would be the largest boulders in the curtain.

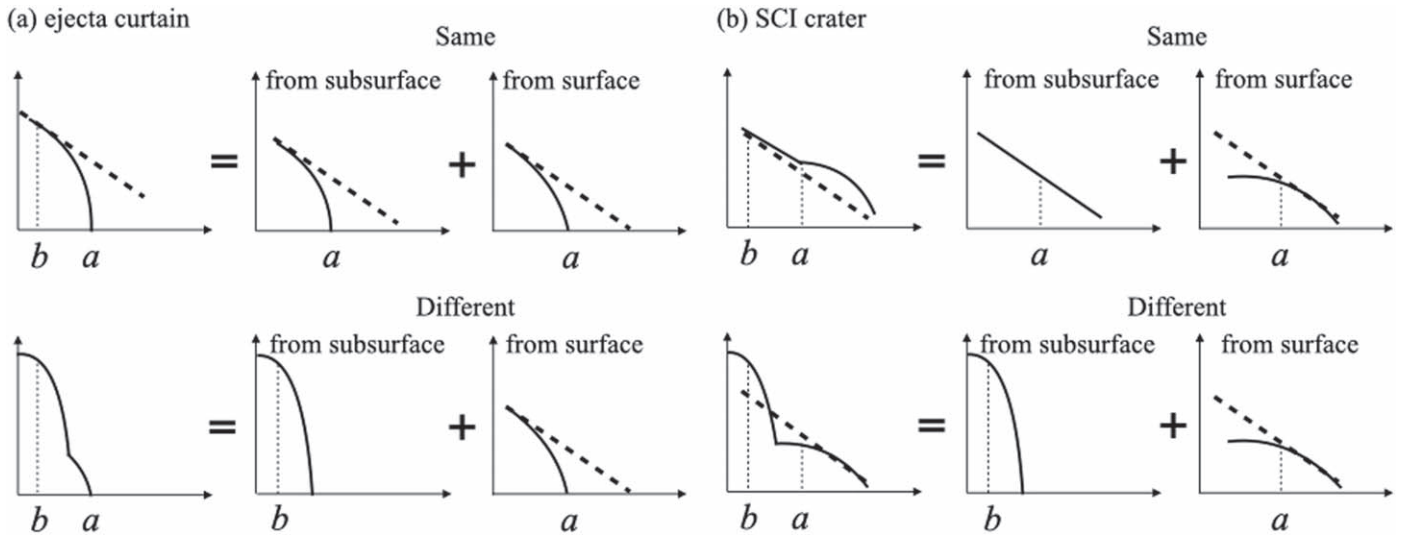


**Figure 3.** Expected cumulative size–frequency distributions of the boulders and the regolith grains (a) in the ejecta curtain and (b) inside the SCI crater. The upper and lower panels in (a) and (b) show the cases that the size distributions in the subsurface and on the surface are the same (a power law indicated by a dashed line) and different, respectively. The observations suggested that the boulders larger than  $a \sim$  several decimeters were not ejected but remained inside the SCI crater and that the ejecta curtain consisted of the regolith grains with the sizes of typically  $b \sim$  several centimeters, ranging from  $\sim 1$  mm to several decimeters. The distributions in the upper and lower panels in (a) are both consistent with the observations. On the other hand, in (b), the distribution in the upper panel is inconsistent with the observed number densities inside the SCI crater (Figure S5A in Arakawa et al. 2020), while the distribution in the lower panel is consistent.

## 4. Discussion

### 4.1. Structure beneath the SCI Impact Point

Filament structure of the SCI ejecta curtain suggests that a size difference between large boulders and small regolith grains in the curtain was at least one order of magnitude. Because the sizes of the largest boulders in the ejecta curtain were observed to be several decimeters, the sizes of the smaller regolith grains in the curtain were likely less than several centimeters. Furthermore, Wada et al. (2020) found that the regolith grains with sizes of several centimeters mainly contributed to the optical thickness of the ejecta curtain (the number of fine grains smaller than  $\sim 1$  mm was not relatively so large that they played a major role in the optical depth of the curtain). Therefore, it is likely that the sizes of the regolith grains in the ejecta curtain were typically several centimeters, ranging from  $\sim 1$  mm to several decimeters.

Arakawa et al. (2020) proposed that there were three layers beneath the SCI impact point: noncohesive surface and subsurface layers and a cohesive basement layer. The ejecta curtain should include the materials from the surface layer and the subsurface layer. Furthermore, Arakawa et al. (2020) obtained the cumulative size–frequency distributions of the boulders on the SCI crater wall and floor. The boulders in the SCI craters are also the mixture of the materials from both layers. The surface layer has been found to consist of boulders having a power-law size distribution (Michikami et al. 2019a; Sugita et al. 2019; Arakawa et al. 2020), while the details of the subsurface layer have not been well known. Here, we evaluated the size distribution of grains in the subsurface layer, based on the constituents in the ejecta curtain obtained above and the boulder size distribution in the SCI crater observed by Arakawa et al. (2020). Figures 3(a) and (b) schematically show expected cumulative size–frequency distributions of the boulders and the regolith grains in the ejecta curtain and inside the SCI crater, respectively. First, we investigated the case that the size distribution of boulders from the subsurface layer was the same as that on the surface of Ryugu (a power-law form). The upper

panels of Figure 3 represent this case. In this case, the number density of boulders in the curtain should be the same power-law form with an upper limit of  $\sim 1$  m (upper panel of Figure 3(a)). For low power-law exponents, the distribution can be consistent with the above distribution in the curtain (Wada et al. 2020). On the other hand, the observed boulders in the SCI crater were the sum of the residual (not ejected) large boulders from the surface and the exposed subsurface boulders. The boulder sizes in the curtain were observed to be less than  $\sim 1$  m; in other words, boulders with a size larger than  $\sim 1$  m remained on the SCI crater floor (e.g., SB and MB). Therefore, the number densities of boulders inside the SCI crater at sizes  $> \sim 1$  m increase while those for  $< \sim 1$  m retain the same power-law form (upper panel of Figure 3(b)). However, the cumulative size–frequency distribution of boulders inside the SCI crater shows that the number densities of boulders  $> \sim 1$  m in diameter are similar to the cumulative size–frequency distribution of the surface boulders and that those for  $< \sim 1$  m are lower than that on the surface (Figure S5A in Arakawa et al. 2020). These differences imply that the size distribution in the subsurface layer was actually different from that on the surface, as suggested by Arakawa et al. (2020).

Then, we consider the case that the size distributions in the subsurface and on the surface are different (lower panels of Figure 3). We suppose that subsurface regolith grains typically had sizes of several centimeters ranging from millimeters to decimeters; the small regolith grains in the ejecta curtain originated from the subsurface (lower panel of Figure 3(a)). In this case, the expected size distribution on the SCI crater wall and floor has the features of the observed distribution such as the lower number densities of boulders  $< \sim 1$  m as shown in the lower panel of Figure 3(b).

Note that, for some natural craters on Ryugu, different size distributions of the boulders inside the craters are recognized in comparison with those on other surfaces of Ryugu (e.g., Cho et al. 2020). This may also result from the different size distribution in the subsurface compared to that at the surface.

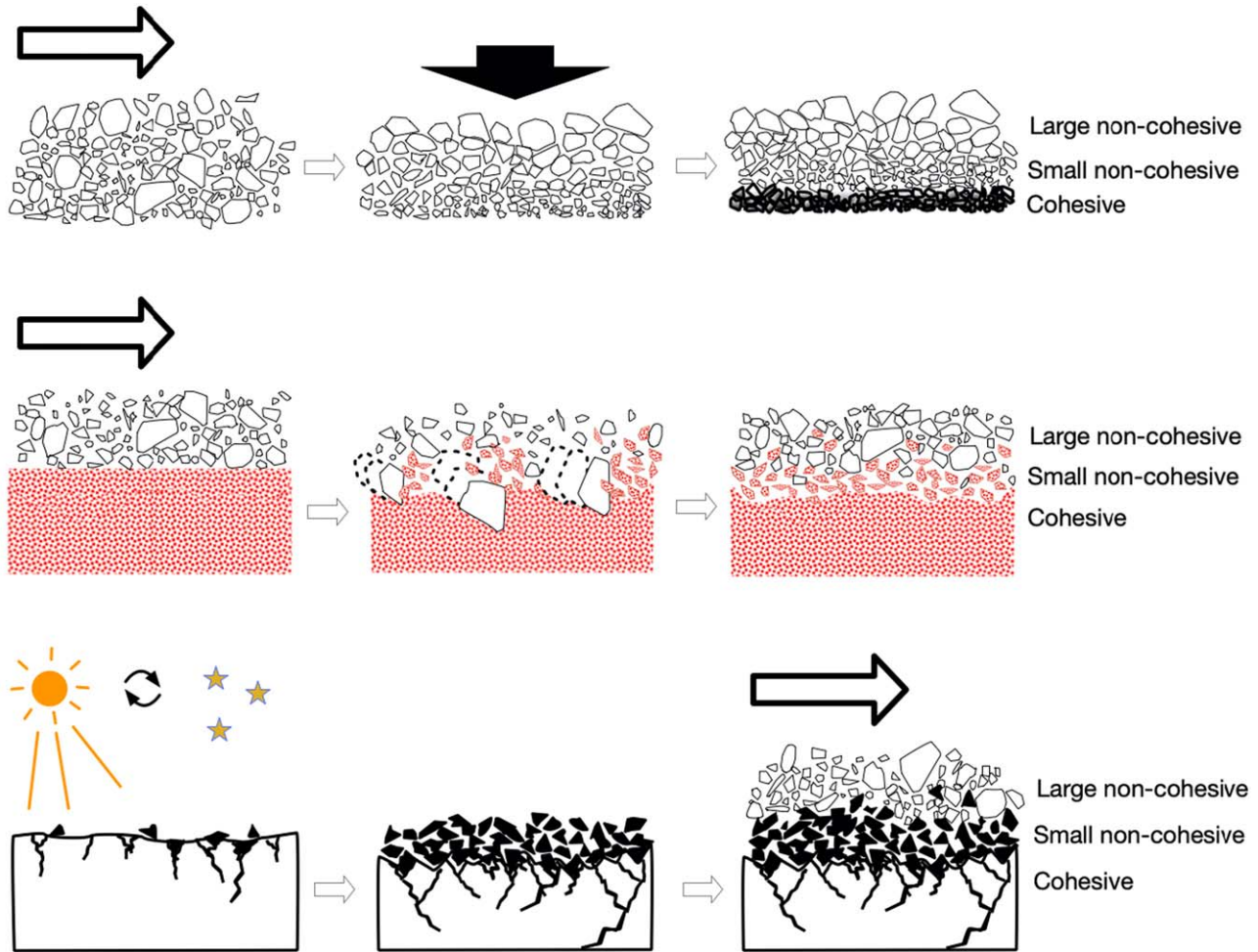


**Figure 4.** Formation process of the structure beneath the SCI impact point. (upper panel) Vertical size segregation model. Segregation occurred in the mass flow, and then small impacts rammed the lower parts, which became a cohesive layer. (middle panel) Scraping model. Mass flow occurred over a weak rock, and large boulders in the flow scraped the weak rock, generating a pile of small fragments as the subsurface layer. (lower panel) Thermal fatigue model. Thermal fatigue by diurnal temperature variation generated small fragments as the noncohesive layer on a large rock, and the strength of the heavily cracked surface of the rock was regarded as a cohesive layer. Mass flow occurred subsequently.

#### 4.2. Formation Process of the Structure beneath the SCI Impact Point

Thus, the structure beneath the SCI impact point can be described as follows. The structure has three layers (Arakawa et al. 2020). The surface layer consists of boulders having a power-law size distribution (Michikami et al. 2019a; Sugita et al. 2019; Arakawa et al. 2020). We show that these boulders have a compressive strength of a few megapascals. We also show that the subsurface layer is consisting of  $\sim$ several-centimeter regolith grains. The basement layer is cohesive, having a compressive strength of  $\sim 500$  Pa, where a pit was formed by the SCI impact (Arakawa et al. 2020). In this section, we propose three hypothetical models to form such a structure. In every model, we assume that the mass wasting from the top of the equatorial ridge to the geopotential lows in the midlatitude regions occurred including the SCI crater region (Sugita et al. 2019).

- (1) Vertical size segregation model (Figure 4, upper panel). In this model, during mass wasting on the surface, vertical convection and size segregation (i.e., Brazil nut effect) occurred as observed in pyroclastic flows (e.g., Mitani et al. 2004), and the size of the boulders vertically

decreased. This structure corresponds to the noncohesive surface and subsurface layers. After this vertical size segregation, numerous small impacts occurred and rammed the lower part of the subsurface layer. This became the solidified basement layer.

- (2) Scraping model (Figure 4, middle panel). In this model, mass wasting of hard boulders occurred over a large buried rock ( $> \sim 10$  m) with a lower mechanical strength (such a weak rock could be breccia or the remnant of an unaltered primitive part of the parent body). We consider the penetration of a hard boulder with a density of  $\rho \sim 10^3$  kg m $^{-3}$  and a size of  $L \sim 1$  m into a large weak rock with a strength of  $P_c \sim 500$  Pa with a velocity  $u$  on the order of the escape velocity of Ryugu,  $\sim 0.1$  m s $^{-1}$ . We suppose that the hard boulder spent its kinetic energy  $\sim \rho L^3 u^2$  crushing the weak rock, i.e.,  $\rho L^3 u^2 \sim L^2 \Delta P_c$ , where  $\Delta$  is the penetration depth, evaluated to be  $\Delta \sim \rho L u^2 / P_c \sim 2$  cm. This implies that such a buried weak rock was scraped and that small fragments with a characteristic size on the order of  $\Delta \sim$  centimeters could be generated; a pile of these fragments would develop between the surface layer and the buried rock as a subsurface layer.

- (3) Thermal fatigue model (Figure 4, lower panel). In this model, thermal fatigue induced by the diurnal temperature variations occurred on a large hard rock ( $> \sim 10$  m; Delbo et al. 2014). The surface of the rock was broken by the thermal fatigue fragmentation and covered with small fragments to form regolith grains as a noncohesive subsurface layer. The local strength of the rock became very low near the surface due to numerous cracks. This part corresponded to the weak basement layer. Then, mass wasting occurred and larger boulders flowed over the fragment layer subsequently.

The properties such as shape and strength of regolith grains in the subsurface are different in each model. The grains should have the characteristic shape of impact fragmentation in model (1) (e.g., an aspect ratio of 2:  $\sqrt{2}$ : 1; Michikami et al. 2019a), which is clearly different from the shape of the fragments generated by thermal fatigue in model (3) (Michikami et al. 2019b). Moreover, the unaltered primitive materials in model (2) would have different physical properties from the surface boulders such as low strength, low density, and high porosity (e.g., 500 Pa and  $0.3 \text{ g cm}^{-3}$ ; Kataoka et al. 2013). Hence, an analysis of the shape and strength of regolith grains in the subsurface layer will indicate the process (1), (2), or (3). The ejecta deposit recovered by the Hayabusa2 sampler from the second touchdown near the SCI crater should include regolith grains from the subsurface. Thus, the sample analysis, such as their strength and shape, will determine which process is the most plausible.

## 5. Summary

The SCI impact experiment was the first-ever impact experiment on an asteroid. The ejecta curtain caused by the SCI impact was observed by DCAM3. The ejecta curtain showed anisotropic and nonuniform patterns. The anisotropic pattern was caused by the large boulder SB, whose compressive strength was estimated to be a few megapascals consistent with a tensile strength (a few hundred kilopascals) estimated based on the thermal inertia measurement by previous studies. The observed nonuniform pattern appearing in the SCI ejecta is consistent with the pattern caused by the variation in the particle sizes in the ejecta curtain in laboratory experiments, implying that the particles in the ejecta curtain had a size range greater than one order of magnitude. The maximum size of the boulders in the ejecta curtain was directly observed to be several decimeters, and the size of small regolith grains in the curtain was estimated to be several centimeters; they interacted with each other, resulting in complex filament (high-contrast) patterns. These constituents in the ejecta curtain and the size distribution of boulders in the SCI crater observed by Arakawa et al. (2020) revealed that the subsurface of Ryugu consisted of the several-centimeter grains.

Thus, we can describe the detailed features of the structure beneath the SCI impact point: a noncohesive surface layer consisting of boulders with a compressive strength of a few megapascals having a power-law size distribution up to several meters, a noncohesive subsurface layer of  $\sim$ several-centimeter regolith grains, and a cohesive basement layer with a compressive strength of  $\sim$ 500 Pa. We proposed three hypothetical models to form such a structure beneath the SCI impact point. An analysis of the properties of the returned samples will indicate which process is the most plausible.

The authors wish to thank all members of the Hayabusa2 team, especially T. Saiki, Y. Imamura, Y. Tsuda, Y. Takagi, M. Hayakawa, H. Yano, C. Okamoto, Y. Mimasu, T. Toda, S. Nakazawa, H. Hayakawa, M. Yoshikawa, and Y. Iijima for promoting the Hayabusa2 mission including the SCI impact operation and the DCAM3 observation; T. Morota, R. Suetsugu, Y. Cho, D. Akabane, and S. Watanabe for useful comments; and M. Koga for producing the figures and supporting the data analysis. The authors are also grateful to an anonymous reviewer for helpful comments. S.S. was supported by Japan Society for the Promotion of Science (JSPS) Core-to-Core Program “International Network of Planetary Sciences.”

## ORCID iDs

Toshihiko Kadono  <https://orcid.org/0000-0002-5299-556X>

## References

- A’Hearn, M., MBelton, M. J. S., Delamere, W. A., et al. 2005, *Sci*, 310, 258  
 Arakawa, M., Saiki, T., Wada, K., et al. 2020, *Sci*, 368, 67  
 Arakawa, M., Wada, K., Saiki, T., et al. 2017, *SSRv*, 208, 187  
 Cho, Y., Morota, T., Kanamaru, M., et al. 2020, *JGRE*, submitted  
 Colaprete, A., Schultz, P., Heldmann, J., et al. 2010, *Sci*, 330, 463  
 Delbo, M., Libourel, G., Wilkerson, J., et al. 2014, *Natur*, 508, 233  
 Grott, M., Knollenberg, J., Hamm, M., et al. 2019, *NatAs*, 3, 971  
 Ishibashi, K., Shirai, K., Ogawa, K., et al. 2017, *SSRv*, 208, 213  
 Kadono, T., Suetsugu, R., Arakawa, D., et al. 2019, *ApJL*, 880, L30  
 Kadono, T., Sugita, S., Sako, S., et al. 2007, *ApJL*, 661, L89  
 Kadono, T., Suzuki, A. I., Matsumura, R., et al. 2020, *Icar*, 339, 113590  
 Kadono, T., Suzuki, A. I., Wada, K., et al. 2015, *Icar*, 250, 215  
 Kataoka, A., Tanaka, H., Okuzumi, S., & Wada, K. 2013, *A&A*, 554, A4  
 Michikami, T., Hagermann, A., Tsuchiyama, A., et al. 2019b, *P&SS*, 177, 104690  
 Michikami, T., Honda, C., Miyamoto, H., et al. 2019a, *Icar*, 331, 179  
 Mitani, N. K., Mattutis, H. G., & Kadono, T. 2004, *GeoRL*, 31, L15606  
 Ogawa, K., Shirai, K., Sawada, H., et al. 2017, *SSRv*, 208, 125  
 Saiki, T., Imamura, H., Arakawa, M., et al. 2017, *SSRv*, 208, 165  
 Schultz, P. H., Hermalyn, B., Colaprete, A., et al. 2010, *Sci*, 330, 468  
 Sugita, S., Honda, R., Morota, T., et al. 2019, *Sci*, 364, 252  
 Wada, K., Ishibashi, K., Kimura, H., et al. 2020, *A&A*, submitted  
 Watanabe, S., Hirabayashi, M., Hirata, N., et al. 2019, *Sci*, 364, 268